Tellus SERIES A DYNAMIC METEOROLOGY AND OCEANOGRAPHY
PUBLISHED BY THE INTERNATIONAL METEOROLOGICAL INSTITUTE IN STOCKHOLM

Tellus (2010), 62A, 333–344

TELLUS

The simulated sea ice thermal microwave emission at window and sounding frequencies

By RASMUS T. TONBOE*, *Danish Meteorological Institute, Lyngbyvej 100, DK-2100 Copenhagen, Denmark*

(Manuscript received 1 September 2009; in final form 13 January 2010)

ABSTRACT

Although the sea ice microwave emissivity is well defined in terms of brightness temperature and the effective temperature it is difficult to derive in practice and its link to physical processes in the snow and sea ice cover is not understood in detail. Future applications of assessing the sea ice microwave emission potentially include atmospheric sounding over sea ice for channels peaking near the surface. Here the microwave emission processes from sea ice are simulated using the combination of a one-dimensional thermodynamic snow and sea ice model and a microwave emission model. The emission model is a sea ice version of the Microwave Emission Model for Layered Snow-packs (MEMLS). It is demonstrated that the simulated seasonal variability of the emissivity, the spectral gradient and the polarization are comparable to satellite measurements. The spectral gradient ratio defined as the difference over the sum of the 18 and 36 GHz at vertical polarization is related to the emissivity at the atmospheric temperature sounding channels at around 50 GHz. Further the brightness temperature at neighbouring channels is highly correlated. However, the effective temperature at lower frequencies (18, 23, 36 and 50 GHz) is poorly correlated with the surface or air temperature.

1. Introduction

For the open ocean we have models describing the water surface microwave emissivity (e) and the sea surface temperature (SST) can be measured by infrared and microwave satellite instruments. These models using surface wind-speed and SST as inputs, are used to compute the sea surface brightness temperature. The simulated surface emission is used when satellite thermal microwave radiance data are assimilated in numerical weather prediction (NWP) models for deriving information on atmospheric temperature and humidity. The satellite data, when assimilated, have an important impact on NWP model skill (e.g. Derber and Wu, 1998; English, 1999).

Transmission of microwave radiation through the atmosphere in the range from 19 to 183 GHz is affected primarily by three processes: (1) oxygen absorption particularly from 50 to70 GHz and near 118 GHz, (2) water vapour absorption near 22 GHz and 183 GHz and (3) scattering from water and ice particles in particular at higher frequencies. Near the 183 GHz water and the 50–70 GHz and 118 GHz oxygen absorption lines the atmosphere is virtually opaque and the satellite channels measuring at or near these frequencies are called sounding channels.

*Corresponding author.
e-mail: rtt@dmi.dk
DOI: 10.1111/j.1600-0870.2010.00434.x

However, there is a potential contribution from the surface at the lower temperature sounding frequencies between 50.3 and 54.4 GHz where microwave penetration is into the troposphere. These frequencies correspond for example to channels 3–6 on the Advanced Microwave Sounding Unit (AMSU) instrument and channels 1–4 on the Special Sensor Microwave Imager/Sounder (SSMIS). The polar atmosphere is generally transparent for microwave radiation in between the sounding channels called the atmospheric windows near 18, 36, 90 and 150 GHz. For typical polar atmospheric states the down-welling emission at the surface is about 5–15 K at 18 GHz, 20–40 K at 36 GHz and 30–100 K at 90 GHz. The sea ice surface emission is typically 150–260 K for comparison. The atmospheric emission is not part of this simulation experiment.

The sea surface emissivity is high compared to the open ocean and penetration through the atmosphere at humidity sounding channels can be significant because the Arctic atmosphere is often very dry. Getting a good estimate of sea ice emissivity is more complicated than over the open ocean. Compared to the open ocean microwave emissivity the complications for sea ice are: (1) the large vertical and lateral surface heterogeneity within the foot-print, (2) the penetration depth and temperature gradient beneath the surface meaning that the surface temperature is not synonymous with the effective temperature and (3) the surface emissivity model input parameters are not prognostic variables in NWP models and they are difficult to simulate.

For sea ice (4–5% of the Earth's surface at any time) there are no operational surface emissivity models. However, English (1999) shows that nearly as much information about atmospheric humidity can be retrieved from, for example, sea ice covered regions as over the open ocean if the emissivity is less than 0.95, the emissivity uncertainty is less than 2%, and the skin temperature uncertainty is less than 2 K. This has been difficult to achieve in practise over sea ice. However, test runs with the regional NWP model HIRLAM where satellite microwave radiometer data from sea ice covered regions were assimilated indicated that atmospheric temperature sounding over sea ice is in fact feasible. The test runs were using a simple sea ice surface emissivity model and it showed that the assimilation of AMSU near 50 GHz temperature sounding data improved model skill on common variables such as surface temperature, wind and air pressure (Heygster et al., 2009).

The sea ice microwave emissivity (e) is well defined in terms of brightness temperature (T_b) and integrated physical temperature (T_{eff}), that is

$$e = T_b/T_{eff}. \quad (1)$$

However, it is difficult to derive in practice and its link to physical processes in the natural snow and sea ice cover is not understood in detail. Therefore, the microwave emission processes from sea ice are simulated here using a one-dimensional thermodynamic sea ice model, with the European Centre for Medium Range Weather Forecast (ECMWF) reanalysis ERA40 input, and a microwave emission model. The ERA40 parameters used as input are: the surface air pressure, the 2 m air temperature, the 10 m wind speed, the incoming short wave solar radiation, the incoming long wave radiation, the dew point temperature, and precipitation. The emission model is a sea ice version of the Microwave Emission Model for Layered Snowpacks (MEMLS) (Wiesmann and Mätzler, 1999). Sea ice dielectric and scattering functions were added to MEMLS in order to simulate the emission processes from sea ice layers beneath the snow. The modifications to the sea ice version are further described in Mätzler et al. (2006) and in Section 2.2.

The question addressed here is, using a combination of thermodynamic and emission modelling: is it feasible to correlate window and sounding channels over sea ice.

The focus is on areas where the ice concentration is near 100% in the Arctic during the cold period from September to May and where the primary variability is due to scattering, snow cover and temperature variations. The thermodynamic model does not handle extended periods of melt, therefore the summer melt period typically from June through August is not considered here. Further, snow metamorphosis on first year ice had to be constrained in the thermodynamic model in order to achieve microwave signatures comparable to measured climatology. The constraining was not necessary for the multiyear ice profiles and emphasis is therefore on the multiyear ice simulations. It is beyond the scope to present a sea ice emissivity model which can readily be implemented in NWP models. Terms such as the surface emissivity and the effective emissivity, the skin or surface temperature, the effective temperature are defined and the sea ice emission processes at frequencies between 18 and 183 GHz at an incidence angle of 50° are mapped. This is similar to the channels and geometry on the SSMIS instrument first launched onboard the defence meteorological satellite program (DMSP) in 2003. SSMIS combines sounding and imaging channels between 19 and 183 GHz with the same imaging geometry on the same platform (Kunkee et al., 2008).

2. The thermodynamic and emission modelling method

The microwave brightness temperature of a lossy half-space such as snow and sea ice is the product of the effective temperature and the emissivity (see eq. 1). The effective temperature is the integrated emitting layer thermometric temperature. Usually, during winter when the atmosphere is colder than the ocean the snow surface temperature is also lower than the effective temperature at the penetration depth. The emissivity at a certain polarization, frequency and incidence angle is a function of subsurface extinction and reflections between layers with different permittivity. The microwave penetration for frequencies higher than 89 GHz is usually confined to the snow cover due to significant extinction in the snow. The ice is saline which leads to a high absorption coefficient thus limiting further penetration. Eppler et al. (1992) noted that during winter, the level first-year ice microwave signatures change primarily due to snow cover related processes. Snow cover is very important for the signature variability of all sea ice types including multiyear ice and new/young ice (Eppler et al., 1992).

2.1. *The combined thermodynamic and emission model*

Combined thermodynamic and emissivity models have the potential to build long snow/sea ice/microwave time-series that can be used for statistical analysis of radiometer sea ice data sensitivities (Mätzler et al., 2006). However, Wiesmann et al. (2000) show that one-dimensional thermodynamic models for snow and frozen ground including microphysical parameters and a vertical stack of layers, for example, SNTHERM (Jordan, 1991) and Crocus (Brun et al., 1989), underestimate the formation of thin crusts or weak layers in the snow pack. Comparison to snow pit measurements showed that the density of thin layers is underestimated in Crocus and thin layers are not represented properly in SNTHERM. Further, when the thermodynamic model output is used as input to a microwave emission model this leads to underestimation of the simulated polarization difference. These models were developed for other applications such as avalanche risk assessment. The thermodynamic model used here treats layers from individual precipitation events and retains all layers even when thin (1 mm) in an attempt to alleviate earlier problems in microwave modelling applications (Tonboe, 2005). Representing the layering in the snow is very important for simulating realistic T_b's and in particular the T_v and T_h polarization difference (Wiesmann et al., 2000). To ensure reasonable initial snow layer thickness precipitation events less than 1 kg m^{-2} over 6 h are retained and released only when the next precipitation event exceeds the threshold. While this may not be totally realistic it does produce simulated snow depths which are comparable to climatology (Warren et al., 1999).

2.2. *The microwave emission model*

Sea ice emission models relate physical snow and ice properties such as density, temperature, snow crystal and brine inclusion size to microwave attenuation, scattering and reflectivity. The model used here is a sea ice version of MEMLS (Wiesmann and Mätzler, 1999) described in Mätzler et al. (2006) and hereafter called the emission model. The theoretical improved Born approximation was used here, which validate for a wider range of frequencies and scatterer sizes than the empirical formulations (Mätzler and Wiesmann, 1999). MEMLS, using an empirical scattering formulation, has earlier been validated for snow on land in the 5–100 GHz region (Wiesmann and Mätzler, 1999). The concern at higher frequencies is the validity of this empirical scattering formulation. The theoretical improved Born approximation is in principle also valid in the 100–200 GHz range and for large scatterers (Mätzler and Wiesmann, 1999). Therefore simulations at 150 and 183 GHz are also presented. Using the improved Born approximation the shape of the scatters is important for the scattering magnitude (Mätzler, 1998). We assume spherical scatters in snow when the correlation length p_{ec}, a measure of grain size, is less than 0.2 mm and the scatters are formed as cups when greater than 0.2 mm to resemble depth hoar crystals. The sea ice version of MEMLS includes models for the sea ice dielectric properties while using the same principles for radiative transfer as the snow model. Again the scattering within sea ice layers beneath the snow is estimated using the improved Born approximation. The scattering in first-year ice and multiyear ice is assumed from small brine pockets and air bubbles within the ice respectively. The emission model is used to simulate the sea ice T_b's and emissivity where the subscript v or h and number denote the polarization at oblique incidence angles and the frequency in GHz, respectively. For example, e_{v89} for the emissivity at 89 GHz and vertical polarization. For the effective temperature (T_{eff}) and the penetration depth only the vertical polarization is presented. The effective emissivity (e_{eff}) which can be derived from measurements using snow surface temperature (T_{surf}) data is computed for verification of the model. All simulations are at 50° incidence angle similar to SSMIS and other conically scanning radiometers. Here, the penetration depth is defined as the depth where the intensity just above the surface has decreased beneath the surface to $1/e$ (0.37) of its initial value. This includes the transmission loss at the surface and at layer interfaces. This definition differs from Hallikainen and Winebrenner (1992) where transmission loss is not included.

2.3. *Sea ice thermodynamic and mass model*

In order to produce input to the emissivity model a one-dimensional snow/ice thermodynamic model has been developed. Its purpose is not necessarily to reproduce a particular situation in time and space rather to provide realistic microphysical input to the emissivity model. Earlier thermodynamic models such as Maykut and Untersteiner (1971) or even simple degree day models (see e.g. Maykut, 1986) are useful for simulating ice thickness. However, for microwave emission modelling applications additional parameters such as temperature, density, snow grain size and ice salinity at very high vertical resolution are needed. Because the thermal conductivity is a function of temperature the model uses an iterative procedure between each time step of 6 h. The thermodynamic model is fed with ECMWF ERA40 data input at these 6 h intervals. In return the thermodynamic model produces detailed snow and ice profiles which are input to the emission model at each time step. This gives a picture of significant emission processes in sea ice even though the one-dimensional thermodynamic model is not capturing the spatial variability of the sea ice cover caused for example by ice convergence resulting in deformation, ice divergence resulting in new-ice formation, and wind redistribution of the snow cover affecting snow depth, density and grain size. The thermodynamic model has the following prognostic parameters for each layer: thermometric temperature, density, thickness, snow grain size and type, ice salinity and snow liquid water content. Snow layering is very important for the microwave signatures therefore it treats snow layers related to individual snow precipitation events. For sea ice it has a growth rate dependent salinity profile. The sea ice salinity is a function of growth rate, u, and water salinity, S_w (Nakawo and Sinha, 1981), that is,

$$S = 0.12S_w/\{0.12 + 0.88\exp(-4.2 \times 10^4 u)\}. \quad (2)$$

The water salinity is 32 psu and the growth rate is in cm d^{-1}.

Climatology indicates that there is snow on multiyear ice at the end of summer melt in September (Warren et al., 1999). Therefore, the multiyear ice simulations are initiated on 1 September with an isothermal 2.5 m ice floe with 5-cm-old snow layer on top. The initial multiyear ice profile is summarized in Table 1. The multiyear ice gradually grows at the six positions from 2.5 m to between 3.0 and 3.4 m in spring and snow depths during winter range between 0.2 and 0.5 m. The melt processes during the summer season are complicated and not sufficiently described by the thermodynamic model. Summer melt is therefore not included in this study. The thermodynamic model is further described in Tonboe (2005).

The seasonal evolution of multiyear ice and first-year ice was simulated separately.

Table 1. The isothermal multiyear ice profile used to initialize simulations on 1 September at the six different multiyear ice positions in the Arctic Ocean. The ice has 5-cm-old snow on top

Layer type and depth beneath the snow surface	Temperature (K)	Density (kg m^{-3})	Correlation length of scatters (mm)	Salinity (ppt)
Snow 0–5 cm	270	300	0.15	0.0
Ice 5–10 cm	270	900	0.35	0.5
Ice 10–25 cm	270	900	0.35	1.0
Ice 25–250 cm	270	910	0.25	2.5

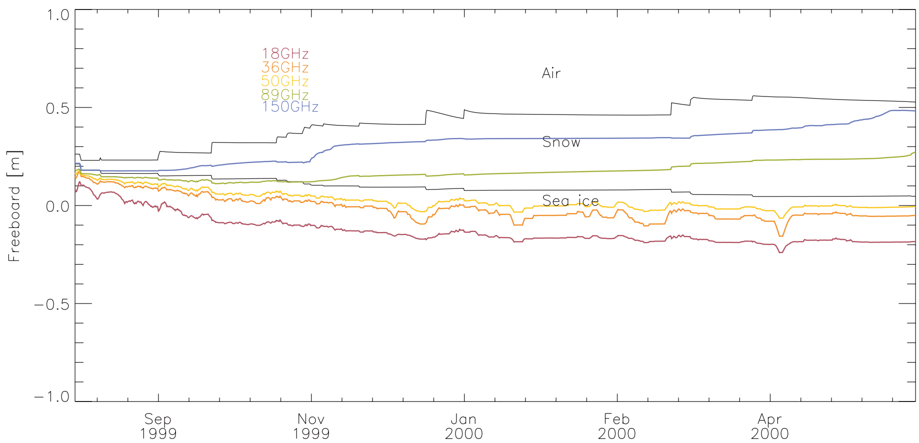

Fig. 1. The simulated snow cover depth on multiyear ice in the Arctic Ocean at 85°N; 0°E between Fram Strait and the North Pole versus time between September 1999 to May 2000. The snow surface and the ice surface is shown with black lines and penetration depth into the snow and ice is shown for 18 GHz with red, 36 GHz with orange 50 GHz with yellow, 89 GHz with green and 150 GHz with blue.

Figure 1 show the simulated snow depth and ice freeboard on multiyear ice in the central Arctic Ocean during the 1999/2000 winter season. Six grid point positions from the ECMWF ERA40 reanalysis were selected in an area north of Greenland which is covered by multiyear ice and other six positions were selected in the Arctic Ocean predominantly covered by first-year ice. The geographic positions of the simulated profiles for both first- and multiyear ice are given in Table 2. These are processed in the same way as the example in Fig. 1 and comprise the total simulated dataset. The simulations begin on 1 September for multiyear ice and on 1 October for first-year ice. September is the beginning of the cold season in the Arctic; however, it is not before October when the vast first-year ice areas North of Siberia freeze up. The first-year ice profiles are initiated with a 1 cm thin ice sheet and a salinity of 8 ppt. Salinity is determined by the model further down in the profile at 5 cm intervals. The first-year reaches ice thickness in spring at the six different positions from 0.9 to 1.6 m and snow depth during winter is between 0.05 and 0.2 m.

2.4. *The interface between the thermodynamic and the emission model*

Snow grain size affects both shortwave extinction in the thermodynamic model and microwave scattering in the emission model. The emission model is using the exponential correlation length

Table 2. Grid point positions for the ECMWF ERA40 meteorological data used as input to the thermodynamic model

First-year ice (latitude, longitude)	Multiyear ice (latitude, longitude)
80.0°N, 120.0°E	85.0°N, 0.0°E
80.0°N, 180.0°E	85.0°N, 300.0°E
82.5°N, 120.0°E	85.0°N, 240.0°E
82.5°N, 180.0°E	87.5°N, 0.0°E
85.0°N, 120.0°E	87.5°N, 300.0°E
85.0°N, 180.0°E	87.5°N, 240.0°E

p_{ec} as a measure of grain size and the optical grain diameter D_0 forms the interface between the two models. There are no snow metamorphosis relationships in terms of p_{ec} so the conversion between terms is needed. It is assumed that grain size and p_{ec} evolve similarly during metamorphosis and our grain size growth model is not dependent on initial grain size. Therefore the conversion factor F is not critical. We use $F = 0.4$ and the correlation length, p_{ec}, of new snow deposits is set to 0.07 mm which is typical for new snow (Wiesmann et al., 1998). Grain growth is not assigned to the top snow layer. Other microphysical parameters in the profile such as physical temperature, density, salinity are used directly in the emission model.

According to Marbouty's (1980) temperature gradient metamorphism model for dry snow, used in the thermodynamic model, the mean grain size diameter (D_m) growth is a function of temperature gradient, temperature and density. Baunach et al. (2001) and Jordan et al. (1999) indicate that the growth rate is also a function of the initial grain size. However, as a first approximation Marbouty's model gives a good fit to observations and for conversion to other structural parameters in the two models it is an advantage that growth rate is independent of initial size. For example, the shortwave extinction in the snow is a function of the snow density and the optical grain diameter (D_0) (Brun et al., 1992). Since growth rate is independent of initial size D_m can be set equal to the diameter of equally sized spheres (D). D is related to D_0 by (Mätzler, 2002), that is,

$$D = D_0(1 - \nu), \tag{3}$$

where

$$\nu = \rho_{snow}/\rho_{ice}. \tag{4}$$

The ρ_{snow} is the snow density and ρ_{ice} is the ice density. The emission model is using p_{ec} a structural parameter of scatter size and distribution (Mätzler, 1998). Mätzler (2002) analyses different relationships between the snow structure, grain size and the correlation length. D_0 is related to p_{ec} for rounded grains, that is,

$$p_{ec} = FD_0, \tag{5}$$

where F is 0.16 for snow grain sizes modelled with SNTHERM, 0.3–0.4 for Crocus grain sizes and types, and 0.16 for fine grained snow and 0.25 for medium grained snow using a one-dimensional scattering model. It is further suggested to include the snow density, that is,

$$p_{ec} = 0.5D_0(1 - \nu). \tag{6}$$

For realistic snow densities between 150 and 400 kg m^{-3} the factor $0.5(1 - \nu)$ is 0.28–0.41, that is, the factor F in eq. (5). These relationships are not strictly valid for new-snow and depth hoar where the grains are not rounded (Mätzler, 2002).

2.5. *Emissivity and effective emissivity*

Since snow–ice temperature profiles are not available on spatial scales covered by airborne microwave radiometers, the skin temperature, which can be measured by infrared radiometers, is often used instead (Hewison and English, 1999; Haggerty and Curry, 2001). Both the effective temperature and the emissivity can also be estimated simultaneously in an optimization scheme (Harlow, 2007). The emissivity derived from measurements using the skin temperature, on a surface, such as sea ice, where the penetration and the temperature gradient are significant, is an effective emissivity (e_{eff}). Table 3 show the temperature gradient computed using the thermodynamic model during the cold season for the snow cover and ice for both first- and multiyear ice. The deposited snow layer is thin on first-year ice. The mean snow depth is 5.3 cm. Together with the relatively thin ice (compared to multiyear ice) this results in a large snow temperature gradient in the snow on first-year ice. The mean $e_{v18} - e_{eff18}$ difference is 0.03 for first-year ice and 0.028 for multiyear ice and the standard deviations (*SD*) are 0.028 and 0.027, respectively. The mean $e - e_{eff}$ difference decreases for higher frequencies as shown in Table 4. The differences between ice types are due to the temperature gradient differences (see Table 3) and penetration depth. The difference between e and e_{eff} is small during a short period in late spring and early summer when the snow–ice is nearly isothermal or during melt where the penetration is limited due to absorption by liquid water. During winter when the surface is most often colder than the snow–ice interior the e_{eff} is higher than e. The computed mean $e_{eff} - e$ differences during the cold season are small compared to the estimate of 0.12 by Harlow (2007) for snow on land. Relatively few campaigns have focussed on sea ice and microwave frequencies above 90 GHz

Table 3. The simulated temperature gradient (dT/dz) in K m^{-1} for snow and ice. The snow dT/dz is the difference between snow surface temperature and the snow–ice interface temperature divided by the snow depth. The ice dT/dz is the difference between the snow–ice interface temperature and the water temperature (271.4 K) divided by the ice thickness

Temperature gradient in snow or ice	First-year or multiyear ice	Mean temperature gradient (K m^{-1})	Temperature gradient *SD* (K m^{-1})
Snow	Multiyear ice	−26.8	25.2
Snow	First-year ice	−142.1	123.7
Ice	Multiyear ice	−5.0	2.8
Ice	First-year ice	−11.8	6.2

Table 4. The simulated mean difference between the e_{effv} for first-year and multiyear ice and 18, 36, 89 and 183 GHz. The e_{effv} is derived from the T_v and T_{surf}

Ice type	Frequency (GHz)	Mean $e_{effv} - e_v$ difference	*SD*
First-year ice	18	0.030	0.028
First-year ice	36	0.029	0.026
First-year ice	89	0.024	0.022
First-year ice	183	0.016	0.014
Multiyear ice	18	0.028	0.027
Multiyear ice	36	0.023	0.022
Multiyear ice	89	0.011	0.011
Multiyear ice	183	0.0045	0.0049

Table 5. The nadir e_{eff} for different sea ice types. Both measurement campaigns are during spring and the T_{surf}, measured with an infrared sensor, is used to derive e_{eff} from T_b

Type	Nadir emissivity				Reference
	24 GHz	50 GHz	89 GHz	157 GHz	
Baltic fast ice (April)	0.872	0.744	0.672	0.696	Hewison and English (1999)
Baltic bare new ice (April)	0.923	0.918	0.910	0.915	Hewison and English (1999)
	37 GHz	90 GHz	150 GHz	220 GHz	
Arctic (May)	0.89	0.73	0.72	0.84	Haggerty and Curry (2001)

(e.g. Hewison and English, 1999; Haggerty and Curry, 2001). Nadir e_{eff} from two campaigns are summarized in Table 5. These measured e_{eff} represent snapshots and the seasonal variability is largely unexplored.

3. Model verification and comparison with measurements

The comparison of e_{eff} mean and *SD* in Fig. 2 shows that the simulated multiyear ice e_{eff} is comparable to the mean e_{eff} derived from satellite SSM/I measurements for multiyear ice at 19, 37 and 85 GHz. The e_{eff} is derived from the SSM/I brightness temperature measurements by dividing the brightness temperature by ECMWF NWP surface temperature fields. Table 6 shows the comparison between measured and simulated emissivity for both multiyear ice e_{effv} and e_{effh}. There is a significant overlap between simulations and measurements even though both the simulated e_{effv} and e_{effh} are from 0.03 to 0.09 higher than the e_{eff} derived from SSM/I measurements. The e_v of the initial profile starting on September 1 is high (see Fig. 1) but it decreases after a few months. Therefore the overestimation is related to the initial profile. However, since the summer season can not be simulated with the thermodynamic model to produce a more realistic autumn profile then the current setup is retained.

The thin snow layer on first-year ice results in a large snow temperature gradient. This temperature gradient is real but this leads in our model to an extreme temperature gradient metamorphosis resulting in depth hoar formation and snow grain size growth. This is, however, not observed in the real world and

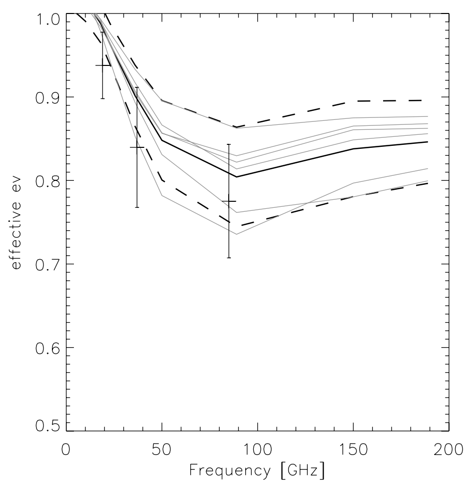

Fig. 2. Frequency versus average e_{eff} for the simulated multiyear ice profiles for October through April. Average ±1 *SD* is shown with dashed lines. Seasonal average (±1 *SD*) e_{eff} derived from SSM/I measurements in the central Arctic Ocean are shown with vertical black bars at 19, 37 and 85 GHz. The simulated average e_{eff} from each of the six multiyear ice profiles is shown with grey lines.

the resulting simulated signatures resemble typical multiyear ice rather than first-year ice. It is speculated that this mismatch between simulated and observed snow cover on first-year ice is due to the continuous wind redistribution of the snow layer on first-year ice which breaks the depth hoar crystals. Wind redistribution and depth hoar breaking is not treated in our thermodynamic model and the simulated first-year ice signatures

Table 6. The mean seasonal simulated and measured e_{eff} and their respective standard deviations. The mean measured and simulated PR_{18} is 0.05 and 0.03, respectively and the $GR_{18/36}$ −0.06 and −0.05, respectively

Frequency	Mean seasonal e_{eff} derived from measurements	Standard deviation of the seasonal e_{eff} derived from measurements	Mean simulated seasonal e_{eff}	Standard deviation of the simulated e_{eff}	Mean difference between measured and simulated e_{eff}
19V	0.94	0.04	0.99	0.02	−0.05
19H	0.85	0.05	0.93	0.02	−0.09
37V	0.84	0.07	0.90	0.04	−0.06
37H	0.77	0.07	0.86	0.04	−0.09
85V	0.78	0.07	0.80	0.06	−0.03
85H	0.72	0.07	0.78	0.06	−0.06

with the extreme metamorphosis are therefore not realistic. The simulations of first-year ice signatures were redone without the temperature gradient metamorphosis (depth hoar formation) and the snow grain size represented by the correlation length, p_{ec}, constrained to 0.1 mm without touching other parameters. This experiment resulted in realistic first-year ice signatures and these second simulations are therefore included in the following for comparison. However, focus is on multiyear ice since it could be simulated without this constraint. Both the gradient ratio and the polarization ratio are parameters often used in sea ice remote sensing and they are used here to verify the model simulations.

3.1. The spectral gradient: a measure of scattering

The spectral gradient ratio (GR) is related to emissivity (Thyness et al., 2005). Brightness temperatures are measured at window frequencies where the sensitivity to the atmosphere is minimized, for example, at 18 and 36 GHz. The GR is given by the following equation:

$$GR_{18/36} = \frac{T_{v36} - T_{v18}}{T_{v36} + T_{v18}}. \quad (7)$$

The normalization reduces the GR sensitivity to thermometric temperature, and ice concentration algorithms use it to correct for first- and multiyear ice types with different scattering magnitudes (Comiso et al., 1997). Though the sensitivity to temperature (T_{eff}) is reduced in GR there is still a reminiscent due to different microwave penetration at 18 and 36 GHz across the temperature gradient in snow and ice.

3.2. The polarization ratio: a measure of layering

The polarization ratio is used here to verify if the simulated data compare to measurements with respect to polarization. The polarization ratio (PR) at 18 GHz is

$$PR_{18} = \frac{T_{v18} - T_{h18}}{T_{v18} + T_{h18}}. \quad (8)$$

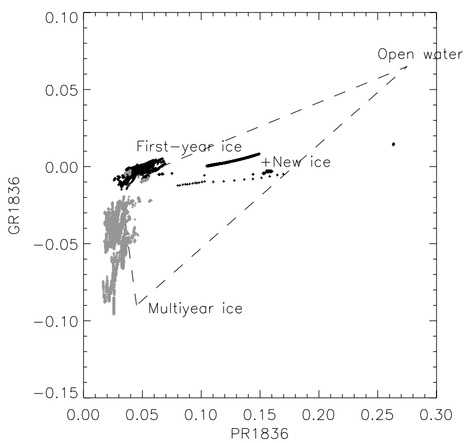

Fig. 3. The simulations for first-year ice and multiyear ice are shown together with tie-points for first-year ice, multiyear ice, open water and new-ice in $GR_{18/36}$ and PR_{18} space. The NASA Team ice concentration retrieval triangle is shown with the dashed line.

The NASA Team ice concentration algorithm is computing the ice concentration in PR_{18} and $GR_{18/36}$ space using typical signatures for open water, first-year ice and multiyear ice called tie-points. 100% sea ice is in this space found along the line between the first- and multiyear ice tie-points. Figure 3 shows the NASA Team ice concentration retrieval space and the triangle spanned by the tie-points with the simulations for first- and multiyear ice. The tie-point for new-ice from Cavalieri (1994) is included for reference. The points cluster close to the tie-points for new-ice, first-year ice and multiyear ice. This shows that at these frequencies (18 and 36 GHz) both the gradient and polarization are realistic. The cluster of points near the new-ice tie-point is snow free thin ice 0.05–0.1 m thick. The polarization ratio decrease and approaches the first-year ice tie-point as soon as snow accumulates and the ice grows thicker (Hwang et al., 2007). The initial multiyear ice profile starts the simulations with signatures near the first-year ice tie-point. As snow accumulates and metamorphosis sets in the simulated multiyear ice points in Fig. 3 come closer to the multiyear ice tie-point. The cluster

Table 7. (A) and (B): The multiyear ice e_v correlation matrix (r^2) is shown in (A). The data set includes all six multiyear ice positions and the whole simulation period (September–May). The first-year ice e_v correlation matrix (r^2) is shown in (B). The dataset includes all six first-year ice profile positions and the whole simulation period (October–May)

	e_{v18}	e_{v23}	e_{v36}	e_{v50}	e_{v89}	e_{v150}	e_{v183}
(A)							
e_{v18}	1.00	0.99	0.98	0.94	0.66	0.33	0.28
e_{v23}	0.99	1.00	0.99	0.96	0.67	0.34	0.28
e_{v36}	0.98	0.99	1.00	0.99	0.74	0.40	0.34
e_{v50}	0.94	0.96	0.99	1.00	0.83	0.51	0.45
e_{v89}	0.66	0.68	0.74	0.83	1.00	0.87	0.82
e_{v150}	0.33	0.34	0.40	0.51	0.87	1.00	0.99
e_{v183}	0.28	0.28	0.34	0.45	0.82	0.99	1.00
(B)							
e_{v18}	1.00	0.95	0.68	0.38	0.05	−0.21	−0.26
e_{v23}	0.95	1.00	0.81	0.57	0.26	−0.03	−0.10
e_{v36}	0.68	0.81	1.00	0.93	0.74	0.44	0.33
e_{v50}	0.38	0.57	0.93	1.00	0.93	0.68	0.58
e_{v89}	0.05	0.26	0.74	0.93	1.00	0.89	0.82
e_{v150}	−0.21	−0.03	0.44	0.68	0.89	1.00	0.99
e_{v183}	−0.26	−0.10	0.33	0.58	0.82	0.99	1.00

of points between the first-year ice and the multiyear ice tie-point resembles measured data points from the Arctic. See for example in Comiso et al. (1997).

4. Simulation results and discussion

Table 7A show the e_v correlation matrix for the six multiyear ice profiles. Ten channels between 18 GHz and 183 GHz are included. On the one hand the e_{v89} in-between the high and lower frequencies has the lowest correlation coefficients (r^2) to its neighbours of all channel emissivities ($r^2 = 0.83$ to e_{v50} and $r^2 = 0.87$ to e_{v150}). It also has the highest span in GHz to its neighbours (39 and 61 GHz) of all channels. On the other hand the four channels between 18 and 50 GHz have high correlation ($r^2 \geq 0.94$) and also the e_{v50} and e_{v150} are highly correlated ($r^2 = 0.99$). The poorer correlation between e_{v89} and the neighbours is not only explained by the large span in frequency to neighbouring channels. At frequencies between 18 and 50 GHz microwave penetration is through the snow into the multiyear ice while penetration at the 150 and 183 GHz is only through the upper part of the snow cover. At 89 GHz penetration is to the snow–ice interface if the snow cover is not too thick and scattering is moderate. The first-year ice e_v correlation matrix is shown in Table 7B. For first-year ice there is no high frequency and low frequency regime as for multiyear ice. The first-year ice e_v is highly correlated ($0.81 \leq r^2 \leq 0.95$) to the e_v from neighbouring channels. However, the correlation decreases much more rapidly than for multiyear ice for next nearest neighbours ($0.57 \leq r^2 \leq 0.82$). In particular the e_{v18} and e_{v23} is poorly correlated with e_{v50} and higher frequency e_v. Some of these emission processes explaining the channel correlations are described as an example for multiyear ice in the following section.

4.1. *Simulated time series showing seasonal multiyear ice e, T_{eff}, penetration depth and snow cover*

Figure 1 (penetration depth versus time) shows the simulated snow accumulation, freeboard and penetration depth at one of the six multiyear ice profiles at 85°N; 0°E between Fram Strait and the North Pole during the 1999/2000 winter season. ECMWF reanalysis data are input to the thermodynamic model. Snow depth increases to about 25–50 cm from September through April at the six different multiyear ice positions. The weight of the snow cover is not completely compensated by the increasing buoyancy of the thickening ice (it grows from 2.5 m to about 3.3 m) which means that the ice freeboard is sinking during winter. The penetration depth at 89 GHz follows the snow–ice interface closely during the first part of the winter while the penetration at 150 GHz is into the upper 10–15 cm of the snow. For the higher microwave frequencies (frequency $\geq$ 89 GHz) penetration is only into the snow cover. The penetration depth in snow is determined by scattering from snow grains and surface reflection processes determined primarily by snow density. For the channels at 18, 36 and 50 GHz penetrating into the multiyear ice the penetration depth variability is linked with the ice temperature. The brine volume of the ice is a function of temperature and ice salinity. The brine volume and the imaginary part of the permittivity decrease as a function of decreasing temperature. When the attenuation decreases then the penetration depth increases and vice versa for higher temperatures. The correlation coefficient between the multiyear ice T_{surf} and the penetration depth is −0.56 at 18 GHz while the correlation is poor but still negative ($r^2 = -0.26$) at 89 GHz where penetration is not into the saline multiyear ice. The variability of the multiyear ice emissivity increases as a function of frequency up to 89 GHz, shown in Fig. 4. The permittivity of snow is a function of its density and temperature. The snow permittivity temperature dependency can be seen in the 50–150 GHz emissivity variations which are coincident with T_{eff} variations to be seen in Fig. 5. The e_{v18} is only changing very little indicating that it is affected mostly by ice and not snow emission processes since the upper multiyear ice salinity and density is not changed during the simulation. The e_{v89} and the e_{v150} are particularly affected by both surface reflection and scattering from the old snow layer at the beginning of the simulation in September. The sharp decrease in emissivity in late October is caused by a shift between scattering models in a 2.6 cm snow layer at 9 cm depth. In the model, when the grain size, represented by the correlation length, is greater than 0.2 mm, then the scatters are assumed to change shape from spheres to cups to represent depth hoar rather than less metamorphosed snow. This change in scattering magnitude

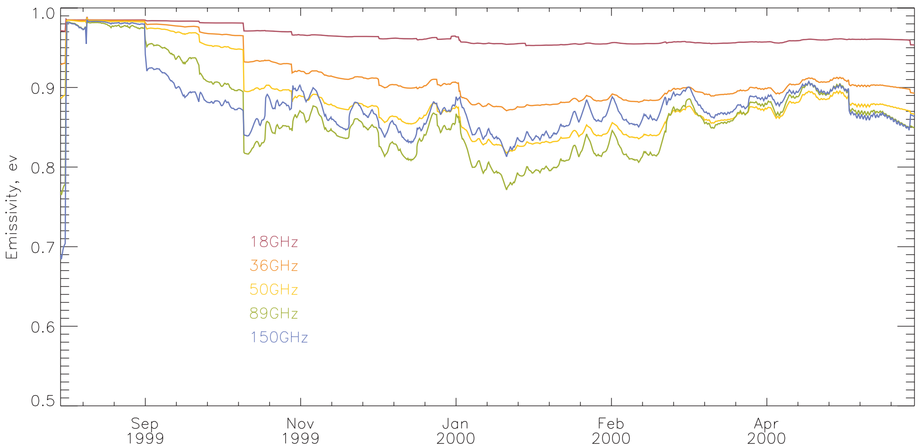

Fig. 4. The simulated e_v for the same profile as in Fig. 1 between September 1999 and May 2000. The curve showing e_{v18} is red, e_{v36} is orange, e_{v50} is yellow, e_{v89} is green and e_{v150} is blue.

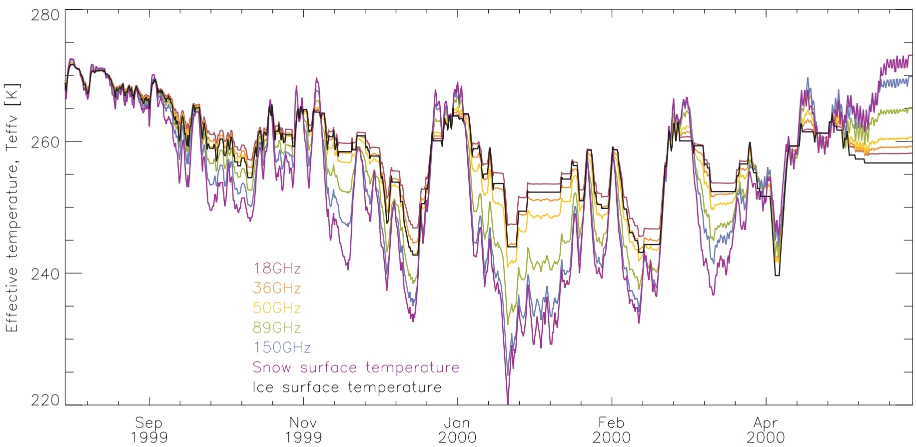

Fig. 5. The simulated T_{eff} for the same profile as in Fig. 1 between September 1999 and May 2000. The curve showing T_{eff18} is red, T_{eff36} is orange, T_{eff50} is yellow, T_{eff89} is green, and T_{eff150} is blue. The T_{surf} is shown with cyan, and the snow–ice interface temperature is shown with black.

reflected in the emissivity affects more the e_{v89} which is penetrating 20 cm than the e_{v150} which is only penetrating 10 cm into the snow at this point. The deeper penetration at 89 GHz than at 150 GHz into the old snow layers above the ice surface with higher scattering decreases the emissivity and explains that e_{v150} is higher than e_{v89}.

The T_{eff} variability is greatest for channels with shallow microwave penetration in the snow layer, that is, T_{eff89} and T_{eff150}. The day to day variations in the T_{eff150} are up to 10 K while the daily snow T_{surf} variations may be up to 15 K. The snow–ice interface temperature at the lower frequencies is correlated with the brightness temperature (not shown). For example the correlation between the multiyear ice snow–ice interface temperature and the T_{v18} is 0.86 for the six profiles. However, the highest correlation between the snow–ice interface temperature and the T_v is around 6 GHz ($r^2 = 0.99$).

4.2. *Interchannel relationships*

Both scattering and snow depth are in particular important for the emissivity and its inter-channel differences. Figure 6 shows the multiyear e_{v89} versus the e_{v150} scatter plot and the linear fit to these emissivities. The channels below 89 GHz generally have penetration into the ice and the channels above 89 GHz have penetration only into the snow surface. 89 GHz in between these two regimes represent much independent information and is relatively poorly correlated to neighbouring channels. In Table 7A the highest correlation of e_{v89} to its neighbours is 0.87, compared to other channels where the maximum correlation to neighbours is 0.99. The correlation between the multiyear ice surface temperature and the air temperature is high (the correlation coefficient is 0.98). However, because of significant penetration, T_{eff} is usually warmer than the surface temperature shown in Fig. 7 for T_{eff89}. In Fig. 7 the first-year ice T_{eff89} is higher than

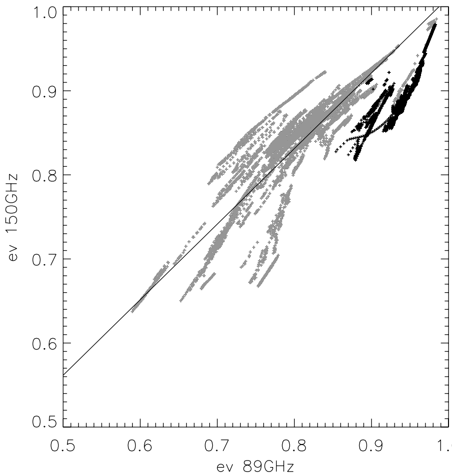

Fig. 6. The simulated e_{v89} GHz versus e_{v150} GHz and the linear fit between the two channels. Multiyear ice is grey and first-year ice is black. The best-fitting line is $e_{v150} = 0.95e_{v89} + 0.11$ for multiyear ice.

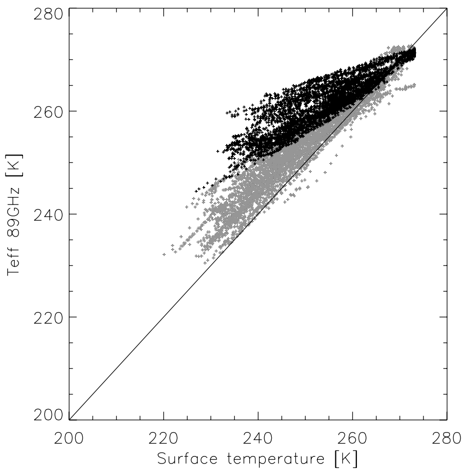

Fig. 7. The simulated T_{surf} versus the T_{eff89}. Multiyear ice is grey and first-year ice is black.

the multiyear ice T_{eff89} because of steeper temperature gradient and shallower microwave penetration in first-year ice than in multiyear ice. Cases where the surface temperature is warmer than T_{eff} coincide with temporary warm spells in winter and atmospheric warming during spring. The first-year ice is warmer than multiyear ice at the 89 GHz penetration depth during winter because of the much higher temperature gradient and thinner ice in first-year ice than in multiyear ice. The correlation between T_{eff89} and the surface temperature is only about 0.6. It is slightly higher for high frequencies and lower for T_b's at low frequencies with significant penetration into the ice. Even though T_{eff} is poorly correlated with the snow surface temperature it's inter channel correlation is high as seen in the next section.

4.2.1. The 50 GHz emissivity. The simulated e_{v36} and e_{v50} is shown in Fig. 8A. For the multiyear ice e_v the points above the line tend to be cases with deep snow while the points below the

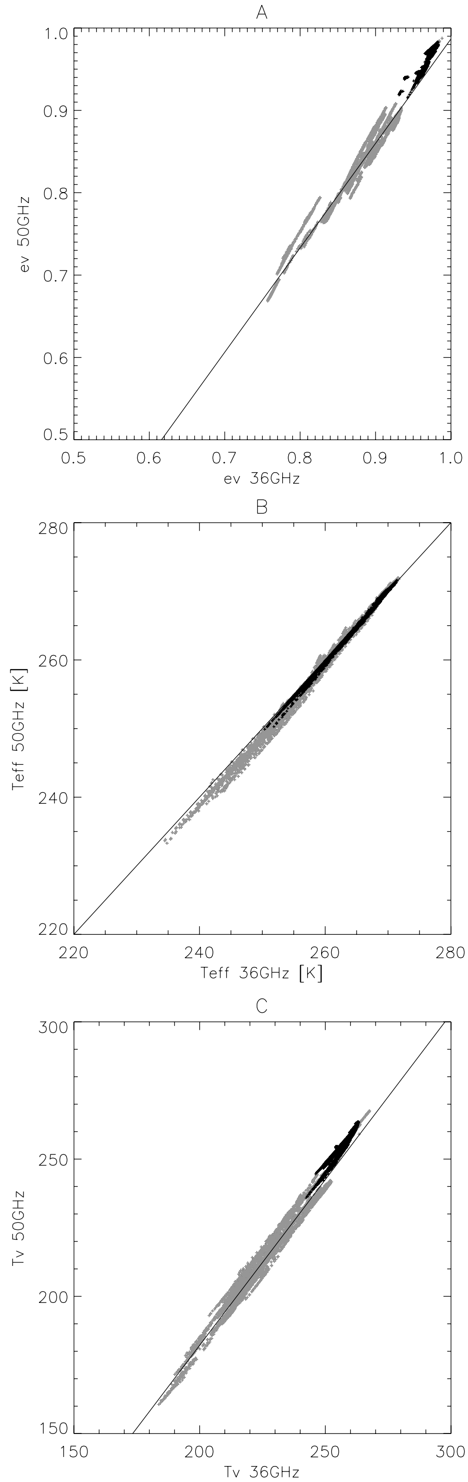

Fig. 8. (A) The simulated e_{v36} versus e_{v50} and the linear fit between the two channels. Grey is multiyear ice and black is first-year ice. The best-fitting line is $e_{v50} = 1.27e_{v36} – 0.28$ for multiyear ice, (B) the simulated T_{eff36} versus T_{eff50}, (C) the simulated T_{v37} versus T_{v50}. The best-fitting line is $T_{v50} = 1.21T_{v36} – 59.2$ for multiyear ice.

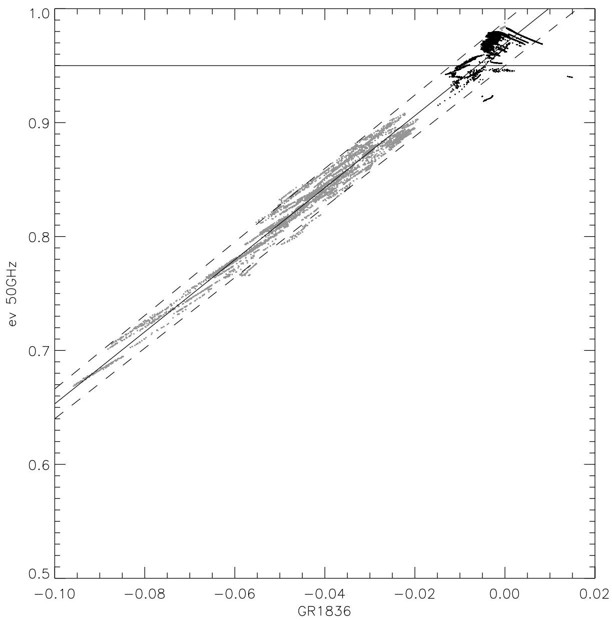

Fig. 9. The simulated e_{v50} versus $GR_{18/36}$. The best-fitting line is $e_{v50} = 3.16GR_{18/36} + 0.97$ for multiyear ice. Grey is multiyear ice and black is first-year ice. The dashed lines show the ±2% around the best-fitting line and the horizontal black line is at an emissivity of 0.95.

line tend to be cases with thin snow. The corresponding T_{eff36} versus T_{eff50} is shown in Fig. 8B where data points have a near one to one correspondence only the T_{eff36} being slightly warmer at low temperatures because of its deeper penetration. In Fig. 8B there is no systematic clustering of the points as a function of snow depth. The brightness temperatures are shown in Fig. 8C. The variability in all three plots is smaller for first-year ice than for multiyear ice and the correlation between neighbouring channels is high (see Table 7A and B). The $GR_{18/36}$ is related to e_{v50} as shown in Fig. 9. English (1999) argues that uncertainties in estimating the surface emissivity of up to ±2% for emissivities below 0.95 could be acceptable limits for atmospheric sounding in NWP models. Nearly all multiyear ice data points are within these limits as shown in Fig. 9. The deviations from the linear fit are functions of several factors. However, the data points above the fitted line tend to be cases with deep snow and small average snow grain size and vice versa for the data points below the line. The first-year ice e_v is generally above the 0.95 line and it is higher than the multiyear ice e_v. The relationship between the multiyear ice $GR_{18/36}$ and the e_{v50} shows that the emissivity is a function of scattering magnitude (represented by $GR_{18/36}$) in the snow and ice.

5. Conclusions

It was demonstrated that the seasonal variability of thermal microwave emission can be simulated using a combination of thermodynamic model and emission modelling. The e_{v18}, e_{v36} and e_{v89}, its temporal variability, the $GR_{18/36}$ and the PR_{18} are comparable to typical signatures derived from satellite measurements. The comparison with satellite derived multiyear ice e_{eff} in Fig. 2 shows that the variability is comparable while the simulated mean is overestimated by 0.03–0.09 at the three frequencies and two different polarizations. However, the ±1 *SD* has a significant overlap between simulated and emissivities derived from satellite measurements. Figure 3 indicate that both the $GR_{18/36}$ and the PR_{18} are comparable to tie-point signatures of first-year ice, new ice and multiyear ice. However, the large cluster of simulated data points between the first-year ice and multiyear ice tie point with relatively high $GR_{18/36}$ values indicate that the scattering magnitude in the initial multiyear ice profile may be underestimated. The correlation between the multiyear ice T_v, e_v and T_{eff} at 18, 36 and 50 GHz is high ($r^2 \geq 0.94$). The correlation between 18 and 36 GHz multiyear ice e_v, T_{eff} and T_v is equally good for high and low physical temperatures. These lower frequencies penetrate into the multiyear ice while the penetration of the 89 GHz is to the snow ice interface. The high frequency channels at 150 and 183 GHz are penetrating the snow surface and the correlation between these is also high ($r^2 = 0.99$). The multiyear ice e_{v89} in between the high and low frequency channels is relatively poorly correlated to its neighbours. For cases with little extinction in the snow the microwave penetration at 89 GHz is to the snow–ice interface. For cases with deeper snow or stronger extinction in the snow the 89 GHz emission is primarily from the snow. The shift between the two emission regimes is very important for the T_{v89} and its correlation to neighbours.

The emissivity is affected by scattering processes in the snow cover and upper ice. The $GR_{18/36}$ which is a measurable proxy for scattering is further related to the multiyear ice e_{v50}. The linear relationship between these two simulated parameters seems robust over a wide range of temperatures and snow depths. However, the T_{eff} relationships to measurable parameters such as air or surface temperature are complicated by the steep temperature gradient near the surface and the penetration depth variability. Nevertheless, it is highly correlated with neighbouring channels. The simulated relationship between $GR_{18/36}$ and e_{v50} suggest that it may be possible to assess the microwave emissivity for atmospheric sounding with satellite measurements seasonally across the Arctic Ocean with microwave instruments such as SSMIS as it is done over open water. Field studies are required to confirm the validity of the $GR_{18/36}$ and e_{v50} relationship. This requires a combination of near surface radiometer measurements at 18, 36 and 50 GHz and detailed snow and ice temperature profiles. It would further be important to study the spatial variability and the effect of wind redistribution of the snow on its metamorphosis and grain size.

6. Acknowledgements

This work was supported by the EU 6th framework programme and IPY project DAMOCLES

(Contract no.: 018509-DAMOCLES). Leif Toudal Pedersen is thanked for valuable comments and discussion. Effective emissivities derived from satellite SSM/I measurements were kindly provided by Catherine Prigent. The constructive comments from two anonymous reviewers improved the manuscript.

References

Baunach, T., Fierz, C., Satyawali, P. K. and Schneebeli, M. 2001. A model for kinetic grain growth. *Ann. Glaciol.* **32**, 1–6.

Brun, E., Martin, E., Simon, V., Gendre, C. and Coleou, C. 1989. An energy and mass model of snow cover suitable for operational avalanche forecasting. *J. Glaciol.* **35**(121), 333–342.

Brun, E., David, P., Sudul, M. and Brunot, G. 1992. A numerical model to simulate snow-cover stratigraphy for operational avalanche forecasting. *J. Glaciol.* **38**(128), 13–22.

Cavalieri, D. J. 1994. A microwave technique for mapping thin ice. *J. Geophys. Res.* **99**(C6), 12561–12572.

Comiso, J. C., Cavalieri, D. J., Parkinson, C. L. and Gloersen, P. 1997. Passive microwave algorithms for sea ice concentration: a comparison of two techniques. *Remote Sens. Environ.* **60**, 357–384.

Derber, J. C. and Wu, W.-S. 1998. The use of TOVS cloud cleared radiances in the NCEP SSI analysis System. *Mon. Wea. Rev.* **126**, 2287–2299.

English, S. J. 1999. Estimation of temperature and humidity profile information from microwave radiances over different surface types. *J. Appl. Meteorol.* **38**, 1526–1527.

Eppler, D. T., Farmer, L. D., Lohanick, A. W., Anderson, M. R., Cavalieri, D. J. and co-authors. 1992. Passive microwave signatures of sea ice. In: *Microwave Remote Sensing of Sea Ice, Geophysical Monograph 68* (ed. F. D. Carsey). American Geophysical Union, Washington, DC, 47–71.

Haggerty, J. A. and Curry, J. A. 2001. Variability of sea ice emissivity estimated from airborne passive microwave measurements during FIRE SHEBA. *J. Geophys. Res.* **106**(D14), 15265–15277.

Hallikainen, M. and Winebrenner, D. P. 1992. The physical basis for sea ice remote sensing. In: *Microwave Remote Sensing of Sea Ice, Geophysical Monograph 68* (ed. F. D. Carsey). American Geophysical Union, Washington, DC, 29–46.

Harlow, R. C. 2007. Airborne retrievals of snow microwave emissivity at AMSU frequencies using ARTS/SCEM-UA. *J. Appl. Meteorol. Climatol.* **46**, 23–35.

Hewison, T. J. and English, S. J. 1999. Airborne retrievals of snow and ice surface emissivity at millimeter wavelengths. *IEEE Trans. Geosci. Remote Sens.***37**(4), 1871–1879.

Heygster, G., Melsheimer, C., Mathew, N., Toudal, L., Saldo, R., and co-authors. 2009. POLAR PROGRAM: Integrated Observation and Modeling of the arctic Sea Ice and Atmosphere. *Bull. Amer. Meteor. Soc.* **90**, 293–297.

Hwang, B. J., Ehn, J. K., Barber, D. G., Galley, R. and Grenfell, T. C. 2007. Investigations of newly formed sea ice in the Cape Bathurst polynya: 2. Microwave emission. *J. Geophys. Res.* **112**, C05003, doi:10.1029/2006JC003703.

Jordan, R. 1991. A one-dimensional temperature model for a snow cover. *CRREL SP* 91–16.

Jordan, R., Andreas, E. and Makshtas, A. 1999. Heat budget of snow covered sea ice at North Pole 4. *J. Geophys. Res.* **104**(C4), 7785–7806.

Kunkee, D. B., Poe, G. A., Boucher, D. J., Swadley, S. D., Hong, Y., and co-authors. 2008. Design and evaluation of the first special sensor microwave imager/sounder. *IEEE Trans. Geosci. Remote Sens.* **46**(4), 863–883.

Marbouty, D. 1980. An experimental study of temperature gradient metamorphosism. *J. Glaciol.* **26**(94), 303–312.

Mätzler, C. 1998. Improved Born approximation for scattering of radiation in a granular medium. *J. Appl. Phys.* **83**(11), 6111–6117.

Mätzler, C. 2002. Relation between grain-size and correlation length of snow. *J. Glaciol.* **48**(162), 461–466.

Mätzler, C. and Wiesmann, A. 1999. Extension of the Microwave Emission Model of Layered Snowpacks to coarse-grained snow. *Remote Sens. Environ.* **70**, 317–325.

Mätzler, C., Rosenkranz, P. W., Battaglia, A. and Wigneron, J. P. eds. 2006. *Thermal Microwave Radiation—Applications for Remote Sensing*. IEE Electromagnetic Waves Series, London, UK.

Maykut, G. A. 1986. The surface heat and mass balance. In: *The Geophysics of Sea Ice* (ed. N. Untersteiner). NATO ASI Series, Plenum Press, New York and London, 395–464.

Maykut, G. A. and Untersteiner, N. 1971. Some results from a time-dependent thermodynamic model of sea ice. *J. Geophys. Res.* **76**, 1550–1575.

Nakawo, M. and Sinha, N. K. 1981. Growth rate and salinity profile of first-year sea ice in the high Arctic. *J. Glaciol.* **27**(96), 315–330.

Thyness, V., Pedersen, L. T., Schyberg, H. and Tveter, F. 2005. Assimilating AMSUA over sea ice in HIRLAM 3D-Var, ITSC XIV Proceedings, Beijing, China 25–31 May 2005.

Tonboe, R. T. 2005. A mass and thermodynamic model for sea ice. Danish Meteorological Institute Scientific Report 05–10, Copenhagen.

Warren, S. G., Rigor, I. G., Untersteiner, N., Radionov, V. F., Bryazgin, N. N., and co-authors. 1999. Snow depth on Arctic sea ice. *J. Clim.* **12**, 1814–1829.

Wiesmann, A. and Mätzler, C. 1999. Microwave emission model of layered snowpacks. *Remote Sens. Environ.* **70**, 307–316.

Wiesmann, A., Fierz, C. and Mätzler, C. 2000. Simulation of microwave emission from physically modelled snowpacks. *Ann. Glaciol.* **31**, 397–404.

Wiesmann, A., Mätzler, C. and Weise, T. 1998. Radiometric and structural measurements of snow samples. *Radio Sci.* **33**(2), 273–289.